Combustion and Flame 287 (2026) 114887

Contents lists available at ScienceDirect

Combustion and Flame

journal homepage: www.sciencedirect.com/journal/combustion-and-flame

Investigation of tangential strain rate impact on NO emissions in turbulent premixed hydrogen flames using the Eulerian Stochastic Fields approach

Antonio Masucci [a,*], Alessandro Porcarelli [b], Tiziano Ghisu [a], Ivan Langella [b]

[a] Department of Mechanical, Chemical and Materials Engineering, Università degli Studi di Cagliari, Via Marengo 2, Cagliari, 09040, Italy
[b] Faculty of Aerospace Engineering, Delft University of Technology, Delft, Netherlands

ARTICLE INFO

Keywords:
Turbulent combustion
Large Eddy Simulation (LES)
Eulerian Stochastic Fields (ESF)
Strain rate
NO emissions
Bluff-body burner

ABSTRACT

Large Eddy Simulations (LES) coupled with the Eulerian Stochastic Fields (ESF) approach are used in this study to investigate the effects of tangential strain on NO emissions. The simulation framework is applied to a lean, hydrogen-air premixed flame stabilised by a conical bluff-body burner developed at the Norwegian University of Science and Technology (NTNU). Simulations are conducted at three different inlet conditions. The inlet mass flow rates of premixed fuel and oxidiser are increased to systematically vary the tangential strain rate and analyse its effect on the flame dynamics and NO formation. The results are validated against experimental measurements, showing good agreement for velocity statistics and flame structure. A detailed analysis reveals that, for the present test case, the tangential strain rate is the dominant contributor to flame stretch, while curvature effects are negligible. Increasing tangential strain enhances flame reactivity up to a critical threshold, beyond which the consumption speed decreases. Results show that increasing the mean tangential strain rate by 24% can lead to an almost 43% reduction in NO emissions per kW. These findings highlight the potential of strain-based control strategies for emission reduction in hydrogen combustion systems and demonstrate the suitability of the ESF method in modelling highly strained, turbulent premixed flames.

Novelty and significance statement

This study provides the first demonstration of how tangential strain rate can be systematically exploited to reduce NO emissions in a practical turbulent premixed hydrogen flame configuration. While previous works have largely focused on laminar counterflow or simplified configurations, this research extends the analysis to a three-dimensional bluff-body stabilised flame, capturing realistic turbulence–chemistry interactions. By employing Large Eddy Simulation coupled with the Eulerian Stochastic Fields (LES–ESF) method, the work achieves a detailed representation of differential diffusion effects and flame–strain coupling without relying on empirical closure assumptions. The findings establish that tangential strain is the dominant contributor to flame stretch, with curvature playing a negligible role, and reveal a critical threshold beyond which increased strain reduces flame consumption speed and NO production. A moderate increase of roughly 24% in mean tangential strain rate was found to yield an almost 43% decrease in NO emissions per unit power. Considering the high tangential strain levels characterising the experimental flame, the results presented here not only demonstrate the robustness of the ESF framework in capturing the trends typical of highly strained hydrogen flames, but also open pathways for strain-based emission control strategies, offering practical relevance for the design of next-generation low-emission hydrogen combustion systems.

1. Introduction

Hydrogen holds tremendous potential as an energy carrier and has emerged as a promising alternative to conventional fossil fuels [1]. In particular, the use of hydrogen in premixed combustion configurations offers the potential for high efficiency and low greenhouse gas emissions. However, the strong reactivity, low ignition energy, and high diffusivity of hydrogen pose significant challenges in controlling flame stability [2–4], making hydrogen more prone to flashback in premixed configurations [5]. Therefore, a fundamental understanding of the physics of hydrogen flames is essential for the design and optimisation of future combustion technologies. Moreover, hydrogen combustion can cause high temperatures, leading to high levels of NO_x when air is the oxidiser. Although NO_x formation can be reduced

* Corresponding author.
E-mail address: antonio.masucci@unica.it (A. Masucci).

https://doi.org/10.1016/j.combustflame.2026.114887
Received 2 September 2025; Received in revised form 19 February 2026; Accepted 23 February 2026
Available online 24 February 2026

by using lean premixed and partially-premixed combustion [6], the aforementioned challenges are further compounded at these conditions due to occurrence of intrinsic instabilities and their synergy with turbulence [7] typical of practical configurations. Large Eddy Simulation (LES) has emerged as a powerful tool for capturing the unsteady dynamics of turbulent reacting flows. LES resolves the large energy-carrying eddies of the turbulent flow field, while the effects of the smaller sub-grid scales (SGS) is modelled. However, the success of LES in reactive flow simulations heavily depends on the accurate representation of sub-grid scale turbulence–chemistry interactions (TCI), which are modelled [8] and remain one of the central challenges in the field. To address the challenge of modelling turbulence–chemistry interaction (TCI), a number of strategies have been developed [9–11]. Flamelet-based formulations, such as the Flamelet Progress Variable (FPV) and Flamelet Generated Manifold (FGM) approaches, are widely adopted in LES of gas turbine combustors and laboratory flames owing to their computational efficiency [12]. These models project the chemical kinetics onto low-dimensional manifolds and typically employ presumed joint probability density functions (PDFs) to represent subgrid-scale scalar fluctuations. However, for hydrogen flames, preferential diffusion effects become significant and must be incorporated by means of additional correction terms in the evolution equations of the controlling variables [13–16]. Thickened Flame (TF) models constitute another commonly used LES strategy, in which the flame front is artificially thickened to permit resolution on the computational mesh, while a subgrid efficiency function accounts for unresolved wrinkling [17–19]. Yet, when applied to hydrogen combustion, TF models may introduce inaccuracies due to the enhanced sensitivity to stretch caused by thickening and their inability to represent thermo-diffusive instabilities. Recent efforts to mitigate these limitations in hydrogen flames can be found in [20–22]. Among these models the transported filtered density function (T-FDF) is well known for its accuracy. By solving a transport equation for the filtered joint density function (FDF) of the thermochemical variables, the FDF method provides a statistically consistent closure for the nonlinear chemical source terms. This removes the need for empirical closure models and enables a more accurate treatment of the combustion process. However, the numerical solution of the FDF transport equation, especially in high-dimensional composition spaces, remains computationally challenging due to the stochastic nature of this equation [23]. An alternative, yet equivalent, approach is the Eulerian Stochastic Fields (ESF) method, where the solution of the FDF transport equation is approximated by a finite ensemble of stochastic fields, each governed by a stochastic partial differential equation [24–26].

In this study, we employ the ESF approach within the context of LES to investigate the behaviour of a premixed hydrogen–air flame stabilised by a bluff-body burner. The flame configuration is based on the experimental setup developed at the Norwegian University of Science and Technology (NTNU) [27] and represents a canonical test case for validating turbulent combustion models. It features a conical bluff body that promotes flame stabilisation by means of flow recirculation, and it is operated under lean conditions with an equivalence ratio of 0.4 and a resulting power of 3.5 kW. The same test case was previously investigated by [28] using the flamelet approach and without including differential diffusion effects. In this work, particular attention is devoted to analyse the coupling between differential diffusion and tangential strain rate and the effects that the latter plays on the local flame structure and NO formation. The tangential strain rate is changed by varying the inlet mass flow rate. As discussed in previous works [29,30], hydrogen addition has been shown to delay the extinction tangential strain rate, proving that hydrogen is able to sustain very high tangential strain rates. A recent study [31] further demonstrated that NO_x emissions can be reduced by increasing the tangential strain rate on the flame front. The study employed a laminar counterflow configuration and it is the objective of this study to extend the work to a 3-D turbulent premixed hydrogen-air flame in a real scenario. Similar effects on the reduction in NO_x emissions linked to tangential strain effects were observed for a turbulent diffusion flame in [32]. The influence of stretch effects on NO_x emissions has been experimentally investigated by Drake et al. [33] showing that the net NO_x formation rates are affected by flame stretch due to changes in peak flame temperature, superequilibrium O atom concentrations, NO destruction reactions, and N_2O formation reactions. In this study, to complement and extend these findings, a premixed configuration is investigated and an extensive description of the relation with NO emission and tangential strain rate is provided. It is worth noting that the amount of NO_2 is significantly smaller than that of NO, and the former can therefore be neglected in the present analysis [34]. Consequently, the trends discussed for NO can be considered representative of the overall NO_x formation.

The objectives of the present study are: (i) to demonstrate the capabilities of ESF-based transported FDF models to predict the coupled strain-differential diffusion effects in lean premixed hydrogen-air flames; and (ii) to investigate the impact that an increase in flame-tangential strain rate has on NO emissions. The first objective is addressed by comparing the experimental measurements against the time-averaged results obtained by LES. The second objective is addressed by first demonstrating that tangential strain effects are predominant over curvature.

Subsequently, the level of tangential strain on the flame is increased by increasing the inlet mass flow rate and then correlated to NO emissions. The paper is structured as follows. The governing equations and combustion modelling are introduced in Section 2. Test cases and configurations are described in Section 3. The numerical details are discussed in Section 4, which is followed by the presentation of the results and their discussion in Section 5. A summary of the work and main conclusions close the paper.

2. Modelling

2.1. 3-D governing equations

The 3-D turbulent simulations are performed using large eddy simulations (LES). The evolution of any given compressible, turbulent reacting flow can be described in a LES via the Favre-filtered governing equations for mass, momentum, energy and species mass conservation. The first two equations are written as follows

$$\frac{\partial \overline{\rho}}{\partial t} + \frac{\partial \overline{\rho}\widetilde{u_i}}{\partial x_i} = 0 \tag{1}$$

$$\frac{\partial \overline{\rho}\widetilde{u_i}}{\partial t} + \frac{\partial \overline{\rho}\widetilde{u_i}\widetilde{u_j}}{\partial x_i} = -\frac{\partial \overline{p}}{\partial x_i} + \frac{\partial}{\partial x_i}\left(\mu \frac{\partial \widetilde{u_i}}{\partial x_i}\right) + \frac{\partial \tau_{sgs,ij}}{\partial x_i} \tag{2}$$

where μ is the dynamic viscosity, $\widetilde{u}_i$ is the ith component of the filtered velocity and $\overline{p}$ and $\overline{\rho}$ are respectively the filtered pressure and filtered density. To close the momentum equation, the Boussinesq hypothesis is used for the unresolved stresses $\tau_{sgs,ij}$. In the context of turbulent reacting flows, a set of N_{sp} further equations needs to be solved for the chemical species involved in the combustion process. The Favre-filtered transport equations for species mass conservation are written in the following form:

$$\frac{\partial \overline{\rho}\widetilde{Y}_k}{\partial t} + \frac{\partial \overline{\rho}\widetilde{u}_i\widetilde{Y}_k}{\partial x_i} = \frac{\partial}{\partial x_i}\left[\left(\overline{\rho}D_k + \frac{\mu_{sgs}}{Sc_{sgs}}\right)\frac{\partial \widetilde{Y}_k}{\partial x_i}\right] + \overline{\dot{\omega}}_k \tag{3}$$

where $\widetilde{Y}_k$ is the Favre-filtered mass fraction of species k, D_k is the diffusivity of species k, Sc_{sgs} is the subgrid Schmidt number set to 0.7 and $\overline{\dot{\omega}}_k$ is the filtered reaction rate of species k. To solve the species mass transport equations, a closure model that takes into account the turbulence-chemistry interaction (TCI) is needed for $\overline{\dot{\omega}}_k$, to be discussed in the next paragraph. An equation for energy is also solved following the sensible enthalpy formulation:

$$\frac{\partial \overline{\rho}\widetilde{h}_s}{\partial t} + \frac{\partial \overline{\rho}\widetilde{u}_i\widetilde{h}_s}{\partial x_i} = -\frac{\partial \overline{p}}{\partial t} + \widetilde{u}_i\frac{\partial \overline{p}}{\partial x_i} + \overline{\dot{\omega}}_T +$$

$$+\frac{\partial}{\partial x_i}\left[\left(\lambda+\frac{\mu_{sgs}C_{p,mix}}{Pr_{sgs}}\right)\frac{\partial\widetilde{T}_k}{\partial x_i}\right]-\frac{\partial}{\partial x_i}\left(\overline{\rho}\sum_{k=1}^{N_{sp}}V_{k,i}\widetilde{Y}_k\widetilde{h}_{s,k}\right)$$

where N_{sp} is the number of species in the reaction mechanism, $Pr_{sgs} = 0.7$ is the subgrid Prandtl number, $\overline{\dot{\omega}}_T$ is the filtered heat release rate and $\widetilde{h}_{s,k}$ is the sensible enthalpy of species k. The Sutherland's transport law is adopted to compute mixture properties such as thermal conductivity λ and dynamic viscosity μ. The mixture specific heat at constant pressure $C_{p,mix}$ is computed from temperature using JANAF polynomials [35]. The diffusivity of each species is modelled using a constant Lewis number approach, resulting in distinct diffusion coefficients for the different species. The diffusion coefficient of species k is thus calculated as:

$$D_k = \frac{\lambda}{\rho\, C_{p,mix}\, Le_k}. \tag{4}$$

Similarly to previous works analysing lean premixed hydrogen flames [7,36] even under intensive strain [37], this approach to account differential diffusion effects is preferred to more expensive transport models to save computational cost as the Lewis number variations across the flame front are typically small [38].

2.2. Combustion model

In reactive flow modelling, the governing equation system is augmented with N_{sp} additional equations to account for the chemical species involved in the combustion process. The general form of the instantaneous transport equation for a chemical species k, represented in terms of its mass fraction Y_k, is given by:

$$\frac{\partial\rho Y_k}{\partial t}+\frac{\partial\rho u_j Y_k}{\partial x_j}=\frac{\partial}{\partial x_j}\left(D_k\frac{\partial Y_k}{\partial x_j}\right)+\dot{\omega}_k \tag{5}$$

Here, ρ denotes the mixture density, u_j is the velocity component in the jth spatial direction, t and x_j represent time and spatial coordinates, respectively, and D_k is the molecular diffusion coefficient of species k.

In this study, the TCI is modelled using the *Transported Filtered Density Function* (T-FDF) method, using the *Eulerian Stochastic Fields* (ESF) formulation. The Favre-filtered density function (FDF), denoted as $\widetilde{P}_{sgs}(\psi;x,t)$, is defined through the convolution of the joint probability density function F with the LES filter function G:

$$\widetilde{P}_{sgs}(\psi;x,t)=\int_V\frac{\rho(x-x')}{\overline{\rho}}\,F(\psi;x',t)\,G(x-x',\Delta(x))\,dx' \tag{6}$$

Letting ψ represent the composition vector of thermochemical scalars ϕ_α, the FDF $\widetilde{P}_{sgs}$ quantifies the probability that the composition vector takes a value within the interval $[\psi,\psi+d\psi]$ inside the LES filter volume V. A corresponding transport equation for $\widetilde{P}_{sgs}$ can be derived [39,40]:

$$\begin{aligned}&\frac{\partial\overline{\rho}\widetilde{P}_{sgs}}{\partial t}+\frac{\partial\overline{\rho u}_j\widetilde{P}_{sgs}}{\partial x_j}+\sum_{\alpha=1}^{N_\alpha}\frac{\partial}{\partial\psi_\alpha}\left(\overline{\rho\dot{\omega}_\alpha}\widetilde{P}_{sgs}\right)=\\&\frac{\partial}{\partial x_j}\left[\overline{\rho}\left(\frac{\overline{\nu}}{Sc}+\frac{\nu_{sgs}}{Sc_{sgs}}\right)\frac{\partial\widetilde{P}_{sgs}}{\partial x_j}\right]\\&-\sum_{\alpha=1}^{N_\alpha}\sum_{\beta=1}^{N_\beta}\frac{\partial^2}{\partial\psi_\alpha\partial\psi_\beta}\left(\overline{\overline{\rho}D\frac{\partial\phi_\alpha}{\partial x_i}\frac{\partial\phi_\beta}{\partial x_i}}\Big|_{\phi=\psi}\widetilde{P}_{sgs}\right)\end{aligned} \tag{7}$$

The left-hand side of Eq. (7) includes the temporal evolution of $\widetilde{P}_{sgs}$, the resolved convection, and the effects due to chemical reactions. Notably, the chemical source term $\dot{\omega}_\alpha$ in the third term of the LHS in Eq. (7) now appears in a closed form and does not require additional modelling. On the right-hand side, the first term accounts for molecular and turbulent diffusion, where ν and Sc are the kinematic viscosity and molecular Schmidt number, respectively. The second term represents molecular (or micro-) mixing, which needs modelling. A common closure for this term is the Linear Mean Square Estimate (LMSE) model [41]. Due to the high dimensionality of the FDF, a deterministic solution of Eq. (7) is computationally prohibitive. To bypass this limitation, the Eulerian Stochastic Fields (ESF) method is employed, which provides a stochastic evolution of the species mass fractions and sensible enthalpy through the FDF of the corresponding fields. In this framework, the FDF is approximated by an ensemble of N_s stochastic fields $\zeta_\alpha^n(x,t)$, with each $\zeta_\alpha^n(x,t)$ representing the nth realisation of the scalar quantity ϕ_α. According to Valino's formulation [25], the evolution of each stochastic field is governed by the following equation:

$$\begin{aligned}&d\overline{\rho}\,\zeta_\alpha^n+\frac{\partial(\overline{\rho u}_i\zeta_\alpha^n)}{\partial x_j}dt-\overline{\rho}\,\dot{\omega}_\alpha^n(\underline{\zeta}^n)dt=\\&=\frac{\partial}{\partial x_j}\left[\overline{\rho}\left(\frac{\overline{\nu}}{Sc}+\frac{\nu_{sgs}}{Sc_{sgs}}\right)\frac{\partial\zeta_\alpha^n}{\partial x_j}\right]dt+\\&+\overline{\rho}\sqrt{\frac{2\mu_{sgs}}{\overline{\rho}Sc_{sgs}}}\frac{\partial\zeta_\alpha^n}{\partial x_j}dW_j^n+\\&-\frac{\overline{\rho}}{2\tau_{sgs}}(\zeta_\alpha^n-\widetilde{\phi}_\alpha)dt\end{aligned} \tag{8}$$

In Eq. (8), the stochastic Wiener process dW_j^n accounts for sub-grid scale fluctuations. The equation incorporates convection, chemical reactions, and both molecular and turbulent diffusion. It is important to note that each stochastic field does not represent a physical realisation of the scalar field; rather, it constitutes a statistically equivalent representation for solving Eq. (7). The final term in Eq. (8) models micro-mixing effects due to viscosity. The sub-grid mixing timescale is defined as $\tau_{sgs} = \Delta^2/(C_d\nu_{sgs})$, where Δ denotes the LES filter width (typically chosen to be the cubic root of the local cell volume in the numerical mesh) and C_d is a model constant, typically set to a value of 2 [42]. The filtered value of any thermochemical scalar ϕ_α is then obtained by ensemble averaging over the stochastic fields:

$$\widetilde{\phi}_\alpha=\frac{1}{N_s}\sum_{n=1}^{N_s}\zeta_\alpha^n \tag{9}$$

In the present study $N_s = 4$ and $N_s = 8$ stochastic fields are used to conduct the validation process. Generally, increasing the number of fields may improve the results but at an increased computational cost [43]. For the present study, it is shown that increasing the number of stochastic fields from 4 to 8 does not significantly affect the results.

2.3. 1-D governing equations

To verify the consistency of the strained flame behaviour as predicted by the ESF approach, the results from the 3-D simulations are also compared with 1-D strained flamelets obtained using a counterflow configuration. One-dimensional simulations are run with the solver CHEM1-D [44]. In one dimension and for a planar reactants-to-products counter-flow flame, the set of conservation equations reads [45]:

$$\frac{\partial\rho}{\partial t}+\frac{\partial\rho u_x}{\partial x}=-\rho K \tag{10}$$

$$\frac{\partial\rho Y_k}{\partial t}+\frac{\partial\rho u_x Y_k}{\partial x}=-\frac{\partial\rho V_{x,k}Y_k}{\partial x}+W_k\dot{\omega}_k-\rho KY_k \tag{11}$$

$$\frac{\partial\rho K}{\partial t}+\frac{\partial\rho u_x K}{\partial x}=\frac{\partial}{\partial x}\left(\mu\frac{\partial K}{\partial x}\right)-\rho K^2 \tag{12}$$

$$\frac{\partial\rho h}{\partial t}+\frac{\partial\rho u_x h}{\partial x}=\frac{\partial q}{\partial x}-\rho Kh \tag{13}$$

where the local stretch rate $K = \frac{\partial u_y}{\partial y}$, the specific absolute enthalpy h and the specific heat flux q, have been introduced. The system is closed with the caloric equation of state and the ideal gas law with a low Mach-number approximation [45]. Differential and preferential diffusion effects are predicted with a mixture-averaged diffusion model.

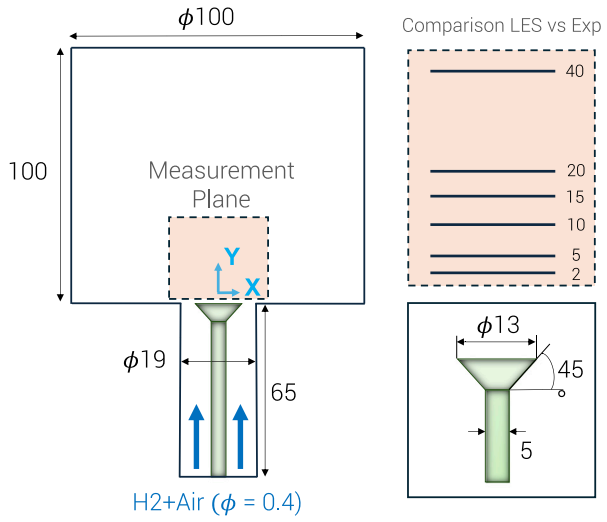

Fig. 1. Schematic of the NTNU premixed hydrogen burner and locations at which comparisons between experimental data and computations are performed for the investigated test case All dimensions are reported in mm.

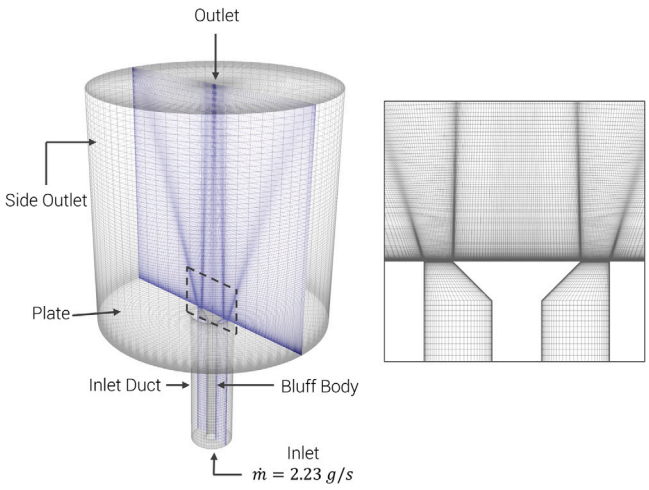

Fig. 2. Computational domain and boundary conditions. A structured mesh was used with a refinement of the grid near the wall in order to solve the boundary layer.

Table 1
Operating conditions for the investigated case. Mass flow rates, the respective theoretical power and mean tangential strain levels are shown for the three different configurations.

	$\dot{m}$ [g/s]	P_{th} [kW]	K_s [1/s]
Case 1	2.29	3.5	11,300
Case 2	3.66	5.5	13,500
Case 3	4.58	6.9	14,000

Table 2
LES boundary conditions used for the investigated case.

Boundary conditions	
Inlet	Mass Flow Inlet
Bluff body	No-Slip wall
Inlet duct	No-Slip wall
Plate	No-Slip wall
Side outlet	Pressure outlet
Outlet	Pressure outlet

3. Case study and operating conditions

The configuration examined in this study is a premixed, bluff-body stabilised H_2-air flame developed at the Norwegian University of Science and Technology (NTNU). A schematic representation of the setup is provided in Fig. 1. The geometry matches the one investigated by [46], with the key distinction that the flame in the configuration analysed here work is unconfined. Comprehensive details regarding the geometry and corresponding experimental measurements can be found in the TNF Workshop database [27].

The burner features a conical bluff body with a diameter 13 mm and a half-cone angle 45°. A hydrogen–air mixture at a temperature $T = 25$ °C is introduced through an annular duct surrounding the bluff-body holder. The outer diameter of the annular duct is 19 mm, while the diameter of the bluff-body holder is 5 mm. The burner operates under unconfined conditions, enabling the flame to develop freely in an environment at atmospheric pressure and room temperature. The mass flow rates of hydrogen and air are $\dot{m}_{H_2} = 2.92 \times 10^{-5}$ kg/s and $\dot{m}_{air} = 2.258 \times 10^{-3}$ kg/s, respectively. The equivalence ratio is maintained at a constant value $\phi = 0.4$. Given the lower heating value $LHV = 120$ MJ/kg, the hydrogen mass flow rate yields to a burner thermal power $P_{\text{th}} = 3.5$ kW. To investigate the effect of tangential strain on NO formation, the total mass flow rate was increased by 60% and 100% relative to the nominal case. These configurations are referred to as *Case 1* (nominal), *Case 2* (60% increase), and *Case 3* (100% increase). The non-reactive case, referred to as *Case N-R*, was performed by imposing only air at the inlet boundary. A summary of the operating conditions and the mean tangential strain levels (explained in the Results section) for all three cases is provided in Table 1.

4. Numerical set-up

4.1. 3-D case

The computational domain begins immediately downstream of a set of three cylindrical rods positioned 65 mm upstream of the bluff-body plane. The open region above the bluff body is represented as a cylindrical volume with a diameter and a height of 100 mm. A schematic of the computational domain and the associated boundary conditions is provided in Fig. 2. The corresponding boundary condition specifications are also summarised in Table 2.

The computational domain was discretised using a mesh comprising approximately 2.5 million hexahedral cells. The mesh near the walls was refined to ensure that the dimensionless wall distance remained below $y^+ = 1.0$. The mesh refinement near the walls also increases cell density in the flame front, as the flame develops close to the edge of the bluff body. Within the reaction zone, cell sizes range from a minimum of 35 μm to a maximum of 400 μm, with an average size of approximately 100 μm. The various axial locations used for comparing the numerical results obtained by the LES with the experimental data of the velocity flow field are those shown in Fig. 1. A mass flow rate boundary condition (implying a constant flat axial velocity profile) was imposed at the inlet, with values corresponding to the operating conditions described earlier (see Table 1). Finally, the mass fractions of the reactants imposed at the inlet were assigned to ensure that the equivalence ratio ($\phi = 0.4$) matched the experimental condition.

The Favre-filtered Navier–Stokes equations for conservation of mass and momentum, are solved together with the transport equations of the Eulerian stochastic fields method (outlined in Section 2.2), where Eq. (8) is used for species mass fractions and sensible enthalpy. The simulations were performed using the finite volume method in OpenFOAM

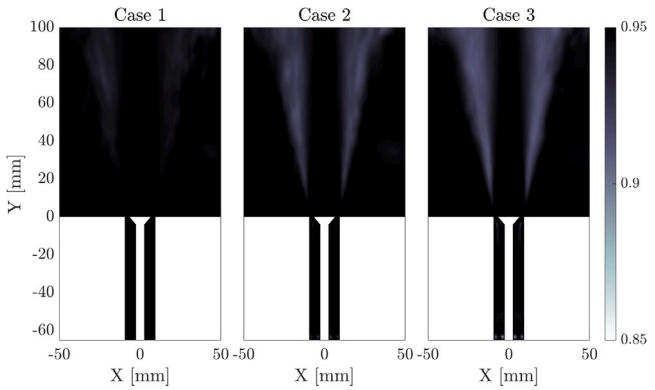

Fig. 3. Contour plot of the Celik criterium for LES quality in the reactive flow simulation for the investigated test cases of Table 1.

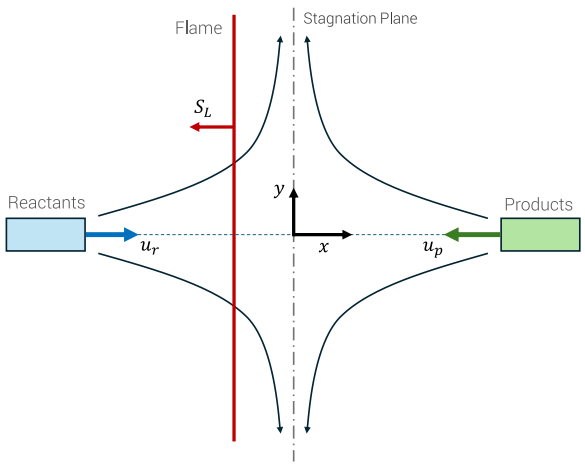

Fig. 4. Schematic of the counterflow configuration employed for the 1-D simulations. u_r and u_p represent respectively the velocity of reactants and products, x and y are respectively the flamelet longitudinal and tangential coordinate, and S_L is the laminar flame speed.

v6. Second-order schemes were selected for both spatial and temporal discretisation. Time steps of 5×10^{-7} s, 3×10^{-7} s, and 2×10^{-7} s were used respectively for Case 1 to 3 to ensure that the CFL number remained below unity in all the domain. The chemical kinetics mechanism in [47] has been combined with the Capurso mechanism [48] to add the NO formation reactions as previously done by Acquaviva et al. [49].

The results were initially validated by comparing the available experimental data with LES results for the nominal mass flow rate (Case 1) using four and eight stochastic fields. To evaluate the ability of the simulations to capture flow characteristics, time-averaged and root-mean-square (RMS) values of the axial and radial velocity components were compared with experimental measurements. The model's capability to predict the flame structure was assessed by comparing the experimental OH* chemiluminescence data obtained through Abel transformation with the filtered heat release rate. The suitability of the mesh for LES simulations was verified by ensuring that at least 80% of the turbulent kinetic energy was resolved. The resolved turbulent kinetic energy spectrum was calculated using the Cèlik criterion [50], where the quality of the mesh is assessed by comparing the ratio of the turbulent and effective viscosity:

$$LES_{IQ} = \frac{1}{1 + 0.05\left(\frac{\nu+\nu_{SGS}}{\nu}\right)^{0.53}} \tag{14}$$

where ν is the kinematic viscosity and ν_{SGS} is the kinematic subgrid viscosity. Results from the reactive flow simulation are presented in Fig. 3, which show that more than 80% of the turbulent kinetic energy is resolved across the entire computational domain for all the three operating conditions. In the present study, Soret effects are neglected to reduce the computational cost of the simulations. While Acquaviva et al. [49] demonstrated the importance of thermal diffusion effects for quantitatively predicting NO emissions in lean premixed and strained hydrogen-air flames, they also showed that the qualitative trends with varying strain rate remain unchanged when these effects are not considered. Thus, neglecting Soret effects is justified in the framework of this work, which investigates NO emission trends as a function of strain in a practical burner configuration.

4.2. 1-D counterflow setup

Results from the 3-D simulations are compared with those from 1-D counterflow simulations conducted at the same equivalence ratio and for varying tangential strain levels in order to assess the capability of the LES approach to predict the expected trends as tangential strain increases. A similar approach was also followed in past studies [7,36]. The same reaction mechanism used for the LES is employed in the 1-D simulations.

The counterflow setup consists of a reactants-to-products configuration, as illustrated in Fig. 4. The reactants mixture, with a nominal equivalence ratio of $\phi = 0.4$, is prescribed on the left-hand side. Following [31], complete combustion products and the unstretched adiabatic equilibrium flame temperature are prescribed on the right-hand side. The applied tangential strain rate in this configuration is defined as

$$K_s = \frac{|u_r| + |u_p|}{L}, \tag{15}$$

where $L = 2$ cm is the domain length, and u_r and u_p are the bulk velocities at the reactants and products boundary, respectively [51]. Three levels of nominal tangential strain rates are considered in this study, corresponding to the ones found in the three turbulent simulations: $K_s = 11{,}300\ s^{-1}$, $K_s = 13{,}500\ s^{-1}$, and $K_s = 14{,}000\ s^{-1}$. Given the applied tangential strain rate (Eq. (15)) and knowing that the same mass flow rate is imposed by CHEM1-D on the reactants and products side, the reactants u_r and products u_p inlet velocities can be found as:

$$u_r = \frac{K_s L}{1 + \frac{\rho_r}{\rho_p}}, \qquad u_p = u_r \frac{\rho_r}{\rho_p}, \tag{16}$$

where the density of the reactants ρ_r and products ρ_p have been introduced.

5. Results and discussion

5.1. Validation

Figs. 5 and 6 present comparisons between LES and experimental data of time-averaged and RMS axial and radial velocity components at various axial positions, for both non-reacting and reacting cases.

The simulations show an overall good agreement with the experimental results for both velocity components and RMS of their fluctuations, except for some underestimation of the radial velocity at 5 and 10 mm. Additionally, a comparison between the axial velocities for the cold and reactive flow cases reveals an increase in the extent of the inner recirculation zone (IRZ) due to the expansion of the gases during the combustion process. Regarding velocity fluctuations, the LES successfully predicts the evolution of the RMS for both axial and radial velocities in the cold flow. However, in the reactive flow case, the RMS of the radial velocity in the shear layer is over-predicted, with a significant over-prediction observed in the central region at

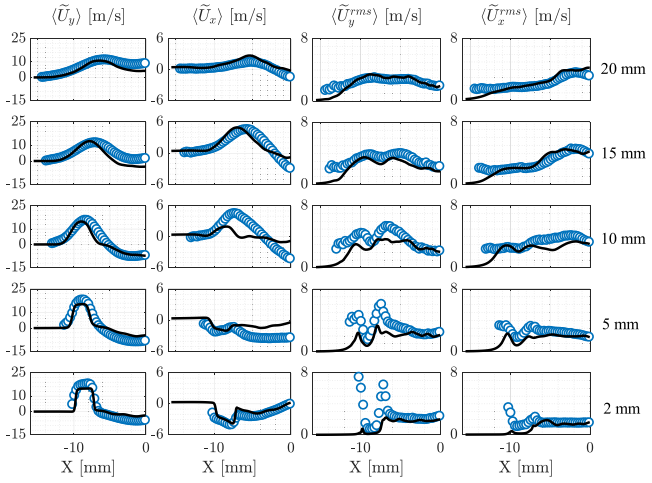

Fig. 5. Radial profiles of time-averaged and RMS axial and radial velocity components at various axial locations from the bluff-body surface, for the non-reacting case (LES: ━, Exp: o).

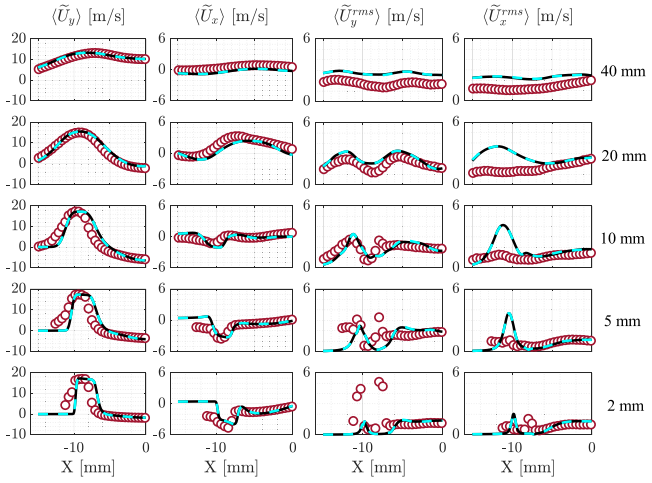

Fig. 6. Radial profiles of time-averaged and RMS axial and radial velocity components at various axial locations from the bluff-body surface, for reacting Case 1 of Table 1: ━, LES 8 stochastic fields: ┈┈, Exp: o).

a height of 20 mm. This over-prediction results from the interaction between flow dynamics and changes in density and composition due to chemical reactions. Discrepancies between the experimental data and the numerical simulation can also be attributed to the limited resolution of the PIV measurements, as noted by Kay et al. [52]. Moreover, it can be observed that an increase in the number of stochastic fields has no effect on the velocity flow field as shown in the results obtained by LES for the reactive case. Nevertheless, these results indicate that the modelling framework investigated here overall is capable of predicting the time-averaged behaviour of the flow behind the bluff-body with relatively good accuracy. Further comparisons with experimental data are shown next. Fig. 7 compares the experimental time averaged OH* chemiluminescence data with the time-averaged filtered heat release rate, both normalised with their maximum value. The figure shows that the LES model is able to capture both the length and the shape of the flame reported in the experimental measurements. An increase in the number of stochastic fields does not lead to significantly different results as observed earlier for the velocity flow field.

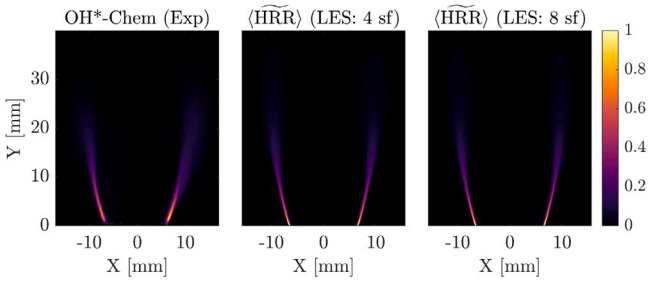

Fig. 7. Time averaged OH*-Chemiluminescence from experiments (left) and midplane contours of time-averaged filtered heat release rate (HRR) from LES results using four (mid) and eight (right) stochastic fields. All plots are normalised by their maximum values.

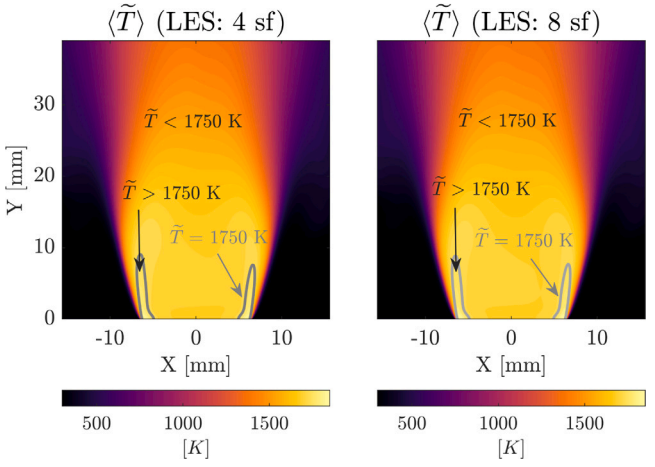

Fig. 8. Time-averaged filtered temperature fields obtained from LES using four (left) and eight (right) stochastic fields. The grey contour corresponds to the 1750 K filtered-temperature isoline. Regions inside the isoline exhibit temperatures higher than 1750 K, whereas regions outside have lower temperatures.

Fig. 8 further presents a comparison of the time-averaged filtered temperature fields obtained using four and eight stochastic fields. First, one can notice that again no significant difference in the LES predictions is obtained when increasing the number of stochastic fields to 8, thus, to limit computational effort, four stochastic fields are used in the remainder of this paper. The results also highlight the presence of differential diffusion effects. For a hydrogen–air mixture at an equivalence ratio of $\phi = 0.4$, the adiabatic flame temperature is approximately 1450 K. However, when flame stretch becomes significant, the local mixture fraction distribution can vary throughout the domain, leading to regions along the flame front that are either richer or leaner than the nominal value. This spatial variation alters the temperature distribution, with localised values exceeding those of a laminar freely propagating flame by more than 400 K at the flame anchoring region (bluff-body base), where stretch effects are expected to be strong due to the presence of the shear layer. Such behaviour is thus captured in the present LES-ESF formulation and the coupling between differential diffusion and tangential strain will be further investigated in the next sections.

Some considerations can be made regarding the micromixing and Wiener terms in Eq. (8). In the shear layer near the flame region, subgrid-scale fluctuations dominate over the micromixing term because the combustion process generates large scalar gradients in this zone. Although the micromixing term depends on the difference between

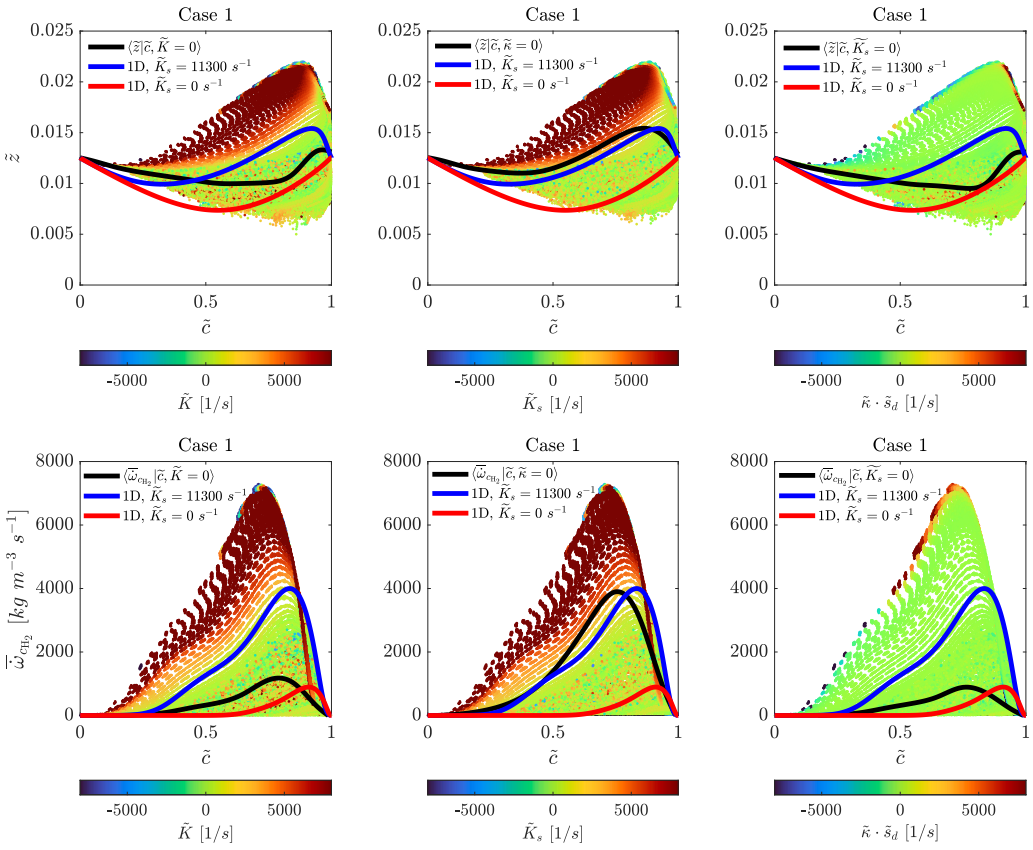

Fig. 9. Scatter plots of mixture fraction (top) and progress variable reaction rate (bottom) versus progress variable in the flame region. Colours represent filtered stretch (left), tangential strain rate (centre), and curvature (right). Solid black lines (—) represent, left to right, the conditional average ($\langle\widetilde{z}|\widetilde{c}\rangle$ or $\langle\widetilde{\omega}_{c_{H_2}}|\widetilde{c}\rangle$) respectively at $\widetilde{K}=0$, $\widetilde{\kappa}=0$ and $\widetilde{K}_s=0$. The progress variable reaction rate from 1-D unstretched premixed flamelet and 1-D counterflow flamelet at the same equivalence ratio are plotted respectively with a solid red line (—) and a solid blue line (—).

each stochastic field and the ensemble mean, its contribution remains limited here since both the cell size and the turbulent viscosity are very small. Further downstream, the scalar gradients weaken while both the cell size and turbulent viscosity increase, leading to a higher relative significance of the micromixing term compared to the Wiener term. These effects are reflected in the standard deviation of the NO stochastic fields, which remains on the order of 2% in the flame region and rises to approximately 13% downstream (not shown), where micromixing effects become more pronounced. Note that, in the absence of experimental or DNS data for the increased-strain cases, the observation of similar strain-dependent trends in the conditional mean of the mixture fraction and the hydrogen-based progress variable indicates that the LES model used here captures the dominant effects of increasing tangential strain rate as expected from DNS studies [31,37]. Yet, the accuracy of LES-ESF in predicting quantitatively species concentrations and NO formation in highly strained turbulent flames should be further assessed in the future as additional data become available.

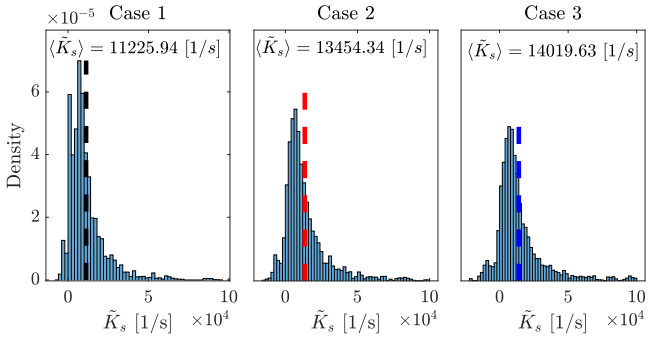

Fig. 10. Probability density function of tangential strain rate. Only reactive samples at $\overline{\omega}_{H_2O} > 1$ are considered. The dashed line represents, from left to right, the mean value of the PDFs respectively for Case 1 (····), Case 2 (····) and Case 3 (····) of Table 1.

5.2. Reacting states

The effect of tangential strain rate on the flow and thermochemical variables is investigated in this section. Stretch, tangential strain, and curvature can be calculated as

$$\widetilde{K} = \widetilde{K_s} + \tilde{s}_d \cdot \tilde{\kappa} \tag{17}$$

$$\widetilde{K_s} = \nabla \cdot \widetilde{u} - \hat{n} \cdot \nabla \widetilde{u} \cdot \hat{n} \tag{18}$$

$$\tilde{\kappa} = \nabla \cdot \hat{n} \tag{19}$$

where K is the total stretch, K_s is the tangential strain, $\tilde{s}_d$ represents the displacement speed and κ is the curvature. The vector $\hat{n} = -\nabla\widetilde{c}_{H_2}/|\nabla\widetilde{c}_{H_2}|$ is the flame-normal vector pointing towards the unburned gas. The displacement speed $\tilde{s}_d$ is calculated as:

$$\tilde{s}_d = \frac{1}{|\nabla\widetilde{c}_{H_2}|}\left(\frac{\partial\widetilde{c}_{H_2}}{\partial t} + \widetilde{u}\cdot\nabla\widetilde{c}_{H_2}\right) \tag{20}$$

Following the analysis in [7], scatter plots of mixture fraction $\tilde{z}$ and hydrogen-based progress variable reaction rate $\overline{\omega}_{c_{H_2}}$ are plotted versus progress variable $\widetilde{c}$ in Fig. 9. These plots are constructed using four random timesteps and are respectively coloured by local values of filtered

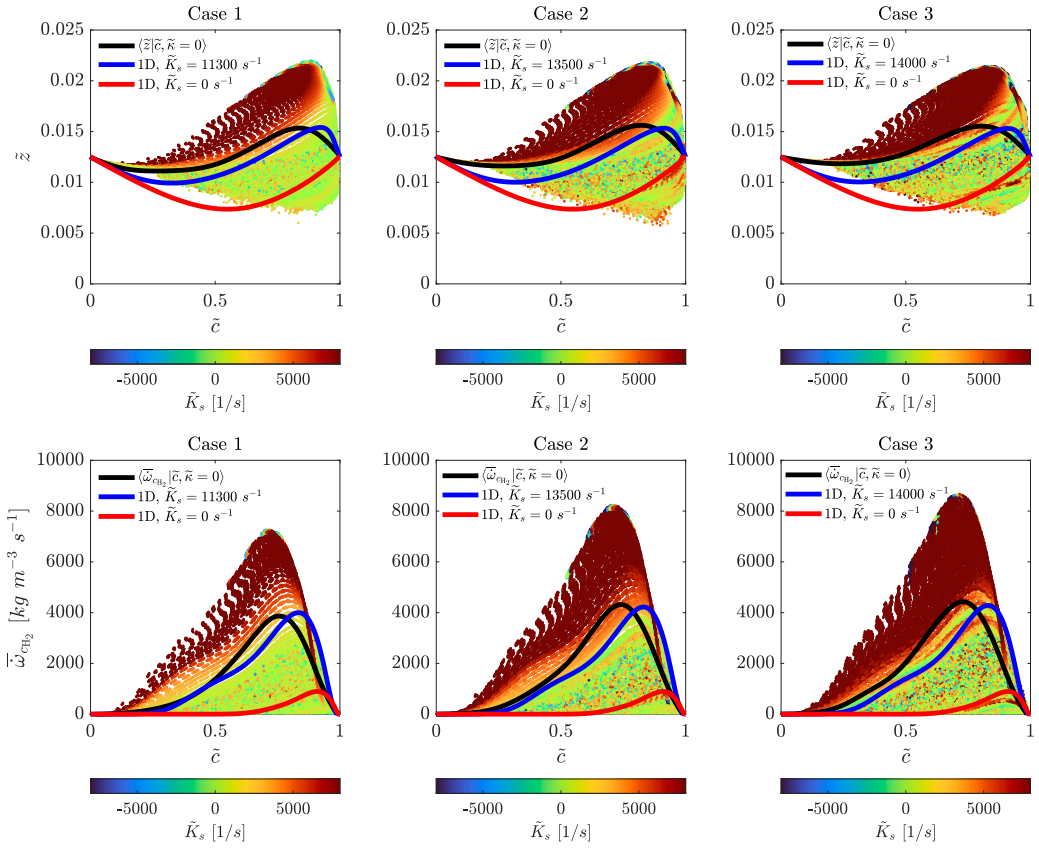

Fig. 11. Scatter plots of mixture fraction (top) and progress variable reaction rate (bottom) versus progress variable in the flame region for the three reacting cases of Table 1. Samples are coloured by filtered tangential strain rate. Solid black lines (—) represent the conditional average ($\langle\tilde{z}|\tilde{c}\rangle$ or $\langle\overline{\dot{\omega}}_{c_{H_2}}|\tilde{c}\rangle$) of samples at $\tilde{\kappa}=0$. The progress variable reaction rate and the Bilger's mixture fraction obtained form the 1-D counterflow and freely propagating (unstretched) simulations at the same equivalence ratio are respectively plotted with solid blue line (—) and solid red line (—).

stretch, tangential strain and curvature. The hydrogen-based progress variable and its source term are defined respectively as $\tilde{c} = 1 - \widetilde{Y}_{H_2}/\widetilde{Y}^u_{H_2}$ and $\overline{\omega}_{c_{H_2}} = -\overline{\omega}_{H_2}/\widetilde{Y}^u_{H_2}$, where $\widetilde{Y}_{H_2}$ represents the filtered hydrogen mass fraction, and the superscript u denotes the unburnt state. To focus on reactive regions, only data points for which $\overline{\omega}_{H_2O} > 1$ are included. By comparing the plots coloured by curvature (right of the figure), for both mixture fraction and progress variable reaction rate, with those coloured by total stretch and strain (respectively left and middle plots in the figure), it becomes evident that the contribution to total stretch of curvature multiplied by $\tilde{s}_d$ is negligible. A similar observation can be made by comparing the conditional mean of mixture fraction at zero stretch (black solid line in the leftmost plot) to that at zero tangential strain (black solid line in the rightmost plot). If curvature effects were significant, one would have expected to observe a local enrichment in the conditional mean at zero tangential strain (black solid line in the rightmost plot) due to curvature effects. However, this is not the case, and an enrichment is instead observed for the conditional mean at zero curvature (black solid line in the central plot), which considers only tangential strain effects. The conditional mean in this case also shows a good agreement with the 1-D counterflow strained flamelet at the same mean tangential strain rate evaluated by means of the PDF of tangential strain (see discussion in the next section).

A similar consideration applies to the scatter plots of the source term of the progress variable, which reveal that both the conditional mean at zero stretch and zero tangential strain rate align with the 1-D unstretched flamelet at the given equivalence ratio. In contrast to the findings of Berger et al. [7], this test case is primarily dominated by tangential strain, and the effects of curvature can thus be neglected. This is an important consideration, as the reduction in NO_x emissions has previously been associated with an increase in tangential strain rate [31]. In the next subsection, the effect of tangential strain will be investigated by increasing its level on the flame via changing the inlet velocity.

5.3. Tangential strain effects on the flame structure

As described in Section 3, the mass flow rate at the inlet is increased by 60% and 100% of the nominal value (respectively Case 2 and Case 3 of Table 1) to impart corresponding increases in the level of tangential strain on the flame. In order to meaningfully compare conditional means from the LES to results obtained from one-dimensional strained flamelets, it is necessary to quantify the level of tangential strain rate on the flame in the turbulent cases. This was accomplished by using data at random timesteps and considering only reacting samples, with the condition $\overline{\omega}_{H_2O} > 1$. Fig. 10 presents the probability density function (PDF) of the tangential strain rate obtained for the three cases. Mean values are also indicated in the figures by the vertical dashed lines. As illustrated in the figure, the mean tangential strain rate increases with the mass flow rate at the inlet. The estimated values of the latter are reported in Table 1 together with the boundary conditions.

It should be noted that comparing the tangential strain levels to those obtained from a laminar computation is not straightforward. In the turbulent case, the presence of transient eddies that appear and vanish rapidly can significantly elevate the strain levels, often resulting

in higher values than in the laminar scenario. Moreover, in laminar simulations, the strain rate is defined as the derivative of velocity with respect to the tangential coordinate. In contrast, in the 3-D turbulent case, the tangential strain on the flame is evaluated using Eq. (18). This mismatch between the two definitions makes it difficult to directly compare the quantities obtained from the 1-D and 3-D simulations. Consequently, estimating the mean tangential strain levels using the probability density function (PDF) provides only an approximation rather than an exact measure. This analysis is therefore performed to estimate a mean level of flame-tangential strain rate in the turbulent cases, and thus have a meaningful comparison with the trends observed in laminar 1D strained flames for the same effective strain. Scatter plots of mixture fraction and progress variable reaction rate versus progress variable are shown in Fig. 11 for the three reacting cases of Table 1, in order to highlight the influence of tangential strain on the flame. As previously discussed, the effects of curvature are assumed to be negligible. The samples in Fig. 11 are coloured according to the tangential strain rate, and the conditional means are calculated assuming zero curvature, thus considering only the effects of tangential strain. The conditional means for each case are compared to the results from the 1-D counterflow strained flamelets at the same mean tangential strain rate, estimated using the PDF (see Table 1). By examining the colour of the samples in both the plots of filtered mixture fraction and progress variable reaction rate, it is evident how the tangential strain levels increase from Case 1 to Case 3. Furthermore, the conditional means for both quantities closely mimic the shape of the laminar counterflow case. Some discrepancies are noticeable in the lean region, where this behaviour is more pronounced in laminar flames compared to the turbulent case. This discrepancy may be attributed to 3-D effects, which are not captured in the 1-D laminar flames. Additionally, the shift in the progress variable reaction rate peak towards lower progress variable values is characteristic of a turbulent flame, and is accurately captured by the combustion model. The top and middle graphs in Fig. 12 presents a comparison between the conditional means of mixture fraction $\tilde{z}$ and progress variable reaction rate $\overline{\dot{\omega}}_{c_{H_2}}$, respectively, obtained from the LES simulations for the three reactive cases reported in Table 1 and the laminar counterflow flames at the same mean tangential strain levels. The conditional means follow the same trends as the 1-D case when the mean tangential strain rate increases. The most notable observation from this figure is that the peak of the reaction rate for the progress variable (middle graphs in Fig. 12) increases with tangential strain, resulting in a more reactive flame. This behaviour is typical for mixtures with a negative Markstein length $\mathcal{L}$. Moreover, the influence of tangential strain rate manifests clearly in the behaviour of the mixture fraction profiles (top graphs in Fig. 12). As the tangential strain rate increases, these profiles become noticeably flatter underscoring the role of tangential strain in limiting thermodiffusive instabilities [36,53]. This effect may also arise because, in the present test case, the increase in tangential strain rate was achieved by increasing the inlet mass flow rate. As a result, however, turbulence intensity also increases (due to the shear gradients), causing turbulent diffusion to dominate over molecular diffusion, thereby limiting the impact of differential diffusion [54].

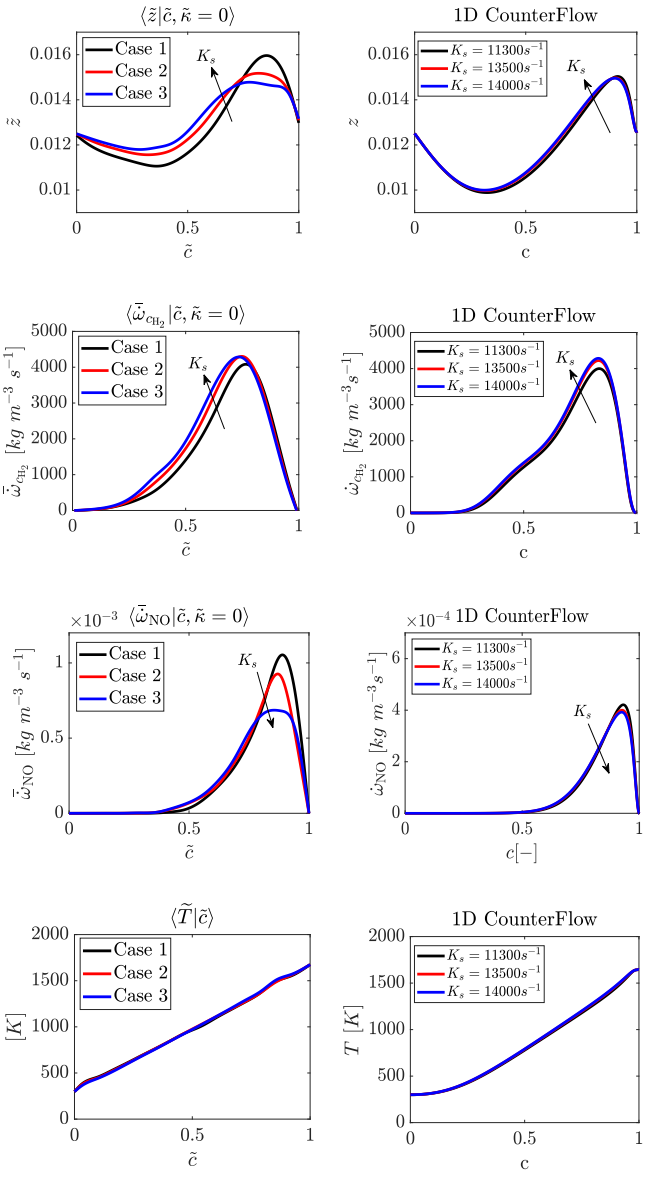

Fig. 12. (Left) conditional means of mixture fraction (first row), reaction rate of hydrogen-based progress variable (second row), reaction rate of NO (third row) and temperature (last row) for the three reactive cases of Table 1 are compared to the same quantities obtained from 1-D counterflow simulations (right) at same conditions of equivalence ratio and mean tangential strain. The arrows indicate the direction of increasing tangential strain rate.

5.4. Tangential strain effects on NO emissions

As discussed in the previous section, higher tangential strain levels lead to an increased reaction rate of the hydrogen-based progress variable. A similar behaviour is expected for the NO reaction rate, as reported by [31]. The latter study showed that although the NO reaction rate increases with tangential strain, a redistribution of OH radicals leads to a decrease in NO emissions as tangential strain increases. In the present work, however, a decrease in the peak NO reaction rate is observed, as shown in the bottom graphs in Fig. 12. This is attributed to a reversal in Markstein length behaviour at sufficiently high tangential strain levels, where the consumption speed begins to decline with increasing tangential strain.

Fig. 13 illustrates this behaviour of the consumption speed, calculated as $S_c = -1/(Y^u_{H_2}\rho^u)\int_{-\infty}^{+\infty}\dot{\omega}_{H_2}dx$, for a 1-D counterflow flame at the same equivalence ratio as the turbulent test case and for increasing strain values. As mentioned earlier, the consumption speed increases with stretch and thus with tangential strain. However, after reaching a level of tangential strain around 12,000 s^{-1}, the consumption speed starts to decrease, following the typical behaviour of a positive Markstein length. This occurs as, despite the peak of $\dot{\omega}_{H_2}$ increases, its integral along the domain decreases due to the flame thickness becoming thinner, and to the fact that strain starts to weaken the flame [55]. By looking at the reaction rate of NO in Fig. 12, one can

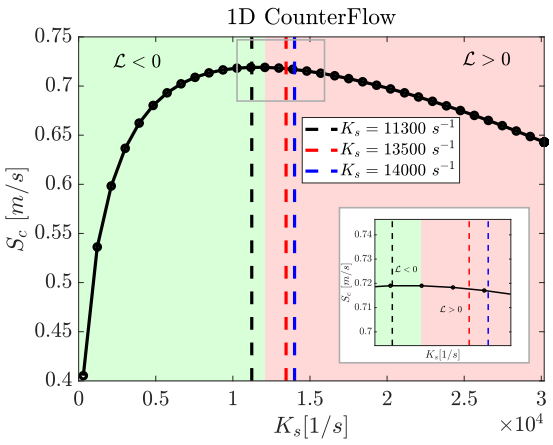

Fig. 13. Consumption speed as function of tangential strain rate in 1-D counterflow simulations at $\phi = 0.4$. The consumption speed increases with tangential strain up to a value of 12,000 s^{-1}. After this value the consumption speed starts to decrease as tangential strain is increased. This transition is highlighted by the inversion of the Markstein length $\mathcal{L}$ which shows the typical behaviour of negative Markestein length mixtures for tangential strain lower than 12,000 s^{-1} and the opposite for tangential strain levels higher than the latter.

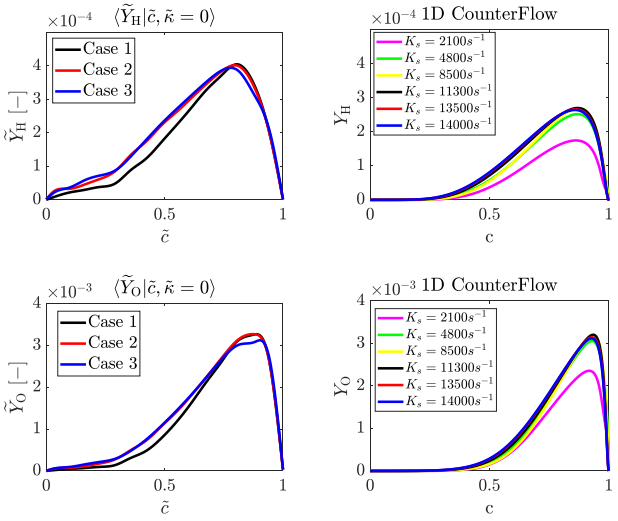

Fig. 14. (Left) conditional means of H (top) and O (bottom) mass fraction for the three reactive cases of Table 1 are compared to the same quantities obtained from 1-D counterflow simulations (right) at same conditions of equivalence ratio and mean tangential strain.

notice that NO formation decreases at sufficiently high tangential strain levels, which is observed for both laminar and turbulent regimes. This occurs because the mean tangential strain rate levels in Case 2 and Case 3 are large enough to induce a shift of the Markstein length from negative to positive.

NO production is also generally influenced by temperature. The plots in the last row of Fig. 12 show the conditional mean of temperature in the progress-variable space (left), together with the corresponding profiles from the laminar counterflow flames (right). As the tangential strain rate increases from Case 1 to Case 3, the conditional mean of temperature does not change significantly, consistent with what is observed in the laminar flames, and in the reaction and product regions it even exhibits a slight increase. This indicates that the reduction in NO is not driven by temperature variations. Porcarelli et al. [31] showed that, in their configuration, the reduction in NO was

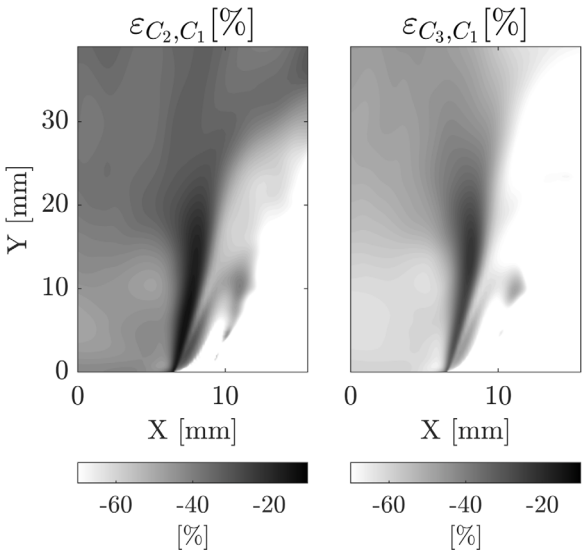

Fig. 15. Relative difference ε in NO mass fraction for Case 2 (left) and Case 3 (right) with respect to Case 1. C_1, C_2 and C_3 in the title of the figure refer to Case 1, Case 2 and Case 3.

linked to the redistribution of OH radicals, which affects NO formation through the thermal route. However, as seen in Fig. 8, the temperatures attained in the present case are too low for the thermal-NO mechanism to dominate. At these temperature levels, the NNH pathway remains the primary route of NO formation, consistent with the findings of Acquaviva et al. [49]. Their study showed that, in laminar counterflow flames, NO peaks increase with strain due to a redistribution of H and O radicals. This behaviour holds in the regime of negative Markstein length. However, when the strain becomes sufficiently high to invert the Markstein length from negative to positive, the redistribution of H and O changes. This behaviour is illustrated in Fig. 14. In laminar counterflow flames, the peaks of both H and O initially increase with strain ($K_s < 11,300\ s^{-1}$), enhancing NO formation through the NNH pathway. Once the strain levels approach those of Case 1, Case 2 and Case 3 ($K_s > 11,300\ s^{-1}$), the peaks start to decrease in the reaction-zone region ($0.8 < c < 1$). A similar trend is observed in the turbulent cases: although H and O increase with strain in the pre-heating region, their peaks decrease in the reaction zone. This reduction directly contributes to the lower NO production via the NNH pathway, in agreement with the behaviour observed in laminar counterflow flames. Fig. 15 shows the local relative difference ε in NO mass fraction calculated as $\varepsilon_{C_i,C_1} = (\langle \widetilde{NO}_{C_i} \rangle - \langle \widetilde{NO}_{C_1} \rangle)/\langle \widetilde{NO}_{C1} \rangle \cdot 100\rangle$ for both Case 2 and Case 3 with respect to Case 1, where C_1 and C_i refer respectively to Case 1 and Case 2 or 3. It can be noted how increasing the tangential strain rate leads to a reduction in NO production both in Case 2 and Case 3. One might object that this decrease could be also attributed to a lower flow residence time because of the increased mass flow rate from Case 1 to Case 2 and 3. However, the NO formation pathway which is strongly affected by the residence time is the thermal one, which is not the dominant pathway in the investigated case, as discussed above. Therefore, this local decrease of NO mass fraction should be solely attributed to strain effects acting across the NNH formation route. The time-averaged mass flow rate of NO, computed as $\overline{m}_{NO} = \int_A (Y_{NO}\ \rho\ U_y)\ dA$, has been further evaluated at the outlet of the LES domain to get a global picture of the NO emissions for the different strain cases.

Given that the mass flow rate of the reactant mixture at the inlet has been increased from Case 1 to Case 3 of Table 1, the thermal power of the burner $P = \dot{m}_{H_2} LHV$ also increases, where $LHV = 120$ MJ/kg denotes the lower heating value of the fuel. To enable a fair

Table 3
From left to right: mass flow rates, the corresponding increase in mean tangential strain, and the reduction of NO mass flow rate normalised by the burner power for the three configurations.

	$\Delta\dot{m}$ %	$\Delta\langle\widetilde{K}_s\rangle$ %	$\Delta(\dot{m}_{NO}/P)$ %
Case 2	+60	+19.5	−26.4
Case 3	+100	+23.9	−42.6

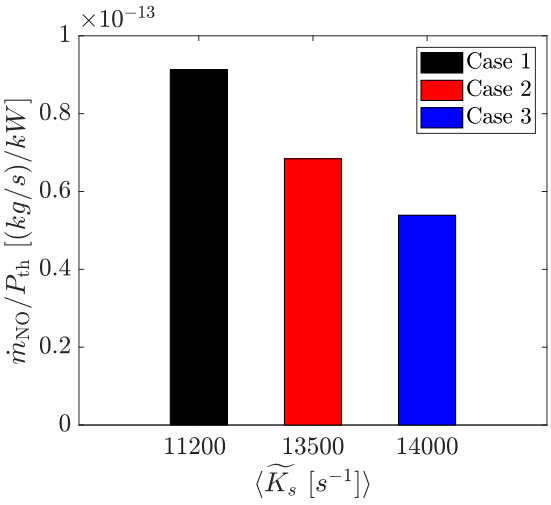

Fig. 16. NO mass flow rate at the outlet divided by the thermal power. The three levels of mean tangential strain rate evaluated using the PDFs are reported on the x direction, showing a decrease in the NO production per kW as the tangential strain rate is increased.

comparison across different operating conditions, the NO mass flow rate is normalised by the burner power, yielding an emission intensity expressed as NO mass flow rate per unit power (in kg/s^{-1}/kW). A similar normalisation approach is used in [48], where an emission index *EI* is defined by dividing the NO mass flow rate by the fuel mass flow rate. This is effectively equivalent to the procedure adopted here, since the fuel mass flow rate is multiplied by the LHV, which remains constant across the three cases while the fuel mass flow rate varies from Case 1 to Case 3. Note that other types of normalisation can also be employed; for instance, one may normalise by the effective power $P_{\text{eff}} = -LHV \int_V \bar{\omega}_{H2} dV$. When using this alternative normalisation (results not shown), the same trends are observed, and the reduction in NO with increasing tangential strain rate remains unchanged. Fig. 16 presents the normalised mass flow rate of NO for each configuration (refer to Table 1) as a function of the mean tangential strain rate. The bar plot illustrates that operating under higher tangential strain conditions leads to a reduction in NO emissions per kilowatt of thermal power. Table 3 reports the percentage reduction in the NO mass flow rate per kW as a function of the percentage increase in the mean tangential strain rate. For increases in the tangential strain rate of 19.5% and 23.9% in Case 2 and Case 3, respectively, compared to Case 1, the mass flow rate per unit kilowatt decreases by 26.4% and 42.6%, respectively, resulting in almost half the NO emissions per kW for Case 3.

6. Conclusions

Large Eddy Simulations of a premixed hydrogen-air flame stabilised by a bluff-body burner were performed to investigate the effects of the coupling between tangential strain and differential diffusion in a premixed burner, and its effect on NO emissions. The simulations employed the Eulerian Stochastic Fields method to account for turbulence-chemistry interactions, with particular emphasis on the role of tangential strain rate in determining flame structure and NO formation characteristics. Three different mass flow rates were examined to systematically vary the tangential strain intensity while maintaining a constant equivalence ratio. The ESF approach, accounting for differential diffusion effects via a non-unity constant Lewis numbers approach, effectively captures the impact of tangential strain evidenced by the redistribution of the mixture fraction and the associated increase in reaction rates. Moreover, the analysis revealed that tangential strain rate is the main component of flame stretch for the investigated case, with curvature contributions being negligible by comparison. This dominance of tangential strain allowed the turbulent flame behaviour to be effectively compared with one-dimensional counterflow strained flamelets. As the mass flow rate and consequently the tangential strain rate was increased, the progress variable source term peak shifted towards higher values, indicating enhanced flame reactivity. The consumption speed was observed to initially increase with tangential strain, exhibiting behaviour characteristic of mixtures with negative Markstein length. However, beyond a critical value of mean tangential strain rate of approximately 12,000 s^{-1}, the consumption speed began to decrease, suggesting a transition in the flame response to tangential strain. A particularly significant finding in the presented analysis is the reduction in NO production at elevated tangential strain rates, demonstrating that the latter can be effectively leveraged to mitigate emissions in hydrogen combustion systems, as hydrogen can sustain high strain levels before extinction. This trend was consistently observed in both the turbulent flame simulations and corresponding laminar flamelet calculations, reinforcing the potential of strain-based approaches to emission control in practical applications. Notably, this study provides the first evidence of NO reduction due to tangential strain effects in a practical premixed hydrogen–air flame configuration. It was shown that doubling the mass flow rate from Case 1 to Case 3 leads to an averaged increase in the flame-tangential strain rate of 23.9%, which in turn results in an almost 43% reduction in NO emissions per kW compared to the nominal case. The results highlight the crucial role of tangential strain in governing both the combustion characteristics and emission formation in bluff-body stabilised hydrogen flames. The demonstrated that it is possible to control NO_x formation through tangential strain manipulation, offering promising avenues for optimising hydrogen combustion systems applications where emissions reduction is critical.

CRediT authorship contribution statement

Antonio Masucci: Writing – review & editing, Writing – original draft, Visualization, Validation, Methodology, Investigation, Formal analysis, Data curation, Conceptualization. **Alessandro Porcarelli:** Writing – review & editing, Writing – original draft, Supervision, Methodology, Formal analysis, Conceptualization. **Tiziano Ghisu:** Writing – review & editing, Writing – original draft, Supervision, Project administration, Funding acquisition, Conceptualization. **Ivan Langella:** Writing – review & editing, Writing – original draft, Supervision, Project administration, Funding acquisition, Formal analysis, Conceptualization.

Declaration of competing interest

The authors declare that they have no known competing financial interests or personal relationships that could have appeared to influence the work reported in this paper.

Acknowledgements

A. Masucci and **T. Ghisu** acknowledge the "e.INS - Ecosystem of Innovation for Next Generation Sardinia" funded by the Italian Ministry of University and Research under the Next-Generation EU Programme (National Recovery and Resilience Plan - PNRR, M4C2, INVESTMENT 1.5 - DD 1056 of 23/06/2022, ECS00000038, CUP F53C22000430001). **A. Porcarelli** and **I. Langella** acknowledge the Dutch Ministry of Education and Science for providing funding support to this project via the Sector Plan scheme. **I. Langella** further gratefully acknowledges financial support from the ERC Starting Grant OTHERWISE, grant n. 101078821.

References

[1] Efstathios-Al Tingas, Hydrogen for Future Thermal Engines, Springer Nature, 2023, http://dx.doi.org/10.1007/978-3-031-28412-0.
[2] B.E. Milton, J.C. Keck, Laminar burning velocities in stoichiometric hydrogen and hydrogen-hydrocarbon gas mixtures, Combust. Flame (ISSN: 0010-2180) 58 (1) (1984) 13–22, http://dx.doi.org/10.1016/0010-2180(84)90074-9.
[3] Zuohua Huang, et al., Measurements of laminar burning velocities for natural gas–hydrogen–air mixtures, Combust. Flame 146 (1) (2006) 302–311, http://dx.doi.org/10.1016/j.combustflame.2006.03.003.
[4] Antonio L. Sánchez, Forman A. Williams, Recent advances in understanding of flammability characteristics of hydrogen, Prog. Energy Combust. Sci. 41 (2014) 1–55, http://dx.doi.org/10.1016/j.pecs.2013.10.002.
[5] Dominik Ebi, Noel T. Clemens, Experimental investigation of upstream flame propagation during boundary layer flashback of swirl flames, Combust. Flame 168 (2016) 39–52, http://dx.doi.org/10.1016/j.combustflame.2016.03.027.
[6] Martin Skottene, Kjell Erik Rian, A study of NOx formation in hydrogen flames, Int. J. Hydrog. Energy 32 (15) (2007) 3572–3585, http://dx.doi.org/10.1016/j.ijhydene.2007.02.038.
[7] Lukas Berger, Antonio Attili, Heinz Pitsch, Synergistic interactions of thermodiffusive instabilities and turbulence in lean hydrogen flames, Combust. Flame 244 (2022) 112254, http://dx.doi.org/10.1016/j.combustflame.2022.112254.
[8] Stephen B. Pope, Turbulent flows, Meas. Sci. Technol. 12 (11) (2001) 2020, http://dx.doi.org/10.1088/0957-0233/12/11/705.
[9] Heinz Pitsch, Large-eddy simulation of turbulent combustion, Annu. Rev. Fluid Mech. 38 (1) (2006) 453–482, http://dx.doi.org/10.1146/annurev.fluid.38.050304.092133.
[10] Tarek Echekki, Epaminondas Mastorakos, Turbulent Combustion Modeling: Advances, New Trends and Perspectives, Springer Science & Business Media, 2010, http://dx.doi.org/10.1007/978-94-007-0412-1.
[11] Denis Veynante, Luc Vervisch, Turbulent combustion modeling, Prog. Energy Combust. Sci. 28 (3) (2002) 193–266, http://dx.doi.org/10.1016/S0360-1285(01)00017-X.
[12] J.A. Van Oijen, et al., State-of-the-art in premixed combustion modeling using flamelet generated manifolds, Prog. Energy Combust. Sci. 57 (2016) 30–74, http://dx.doi.org/10.1016/j.pecs.2016.07.001.
[13] Nithin Mukundakumar, et al., A new preferential diffusion model applied to FGM simulations of hydrogen flames, Combust. Theory Model. 25 (7) (2021) 1245–1267, http://dx.doi.org/10.1080/13647830.2021.1970232.
[14] E.J. Pérez-Sánchez, E.M. Fortes, D. Mira, Assessment of the flamelet generated manifold method with preferential diffusion modeling for partially premixed hydrogen flames, Combust. Flame 277 (2025) 114141, http://dx.doi.org/10.1016/j.combustflame.2025.114141.
[15] Stijn N.J. Schepers, Jeroen A. van Oijen, FGM modeling of thermo-diffusive unstable lean premixed hydrogen–air flames, Combust. Flame (ISSN: 0010-2180) 280 (2025) 114332, http://dx.doi.org/10.1016/j.combustflame.2025.114332.
[16] Hannes Böttler, et al., Flamelet modeling of thermo-diffusively unstable hydrogen-air flames, Proc. Combust. Inst. 39 (2) (2023) 1567–1576, http://dx.doi.org/10.1016/j.proci.2022.07.159.
[17] O Colin, et al., A thickened flame model for large eddy simulations of turbulent premixed combustion, Phys. Fluids 12 (7) (2000) 1843–1863, http://dx.doi.org/10.1063/1.870436.
[18] Jean-Philippe Legier, Thierry Poinsot, Denis Veynante, Dynamically thickened flame LES model for premixed and non-premixed turbulent combustion, in: Proceedings of the Summer Program, vol. 12, Center for Turbulence Research Stanford, CA, 2000, pp. 157–168.
[19] T.D. Butler, Peter J. O'Rourke, A numerical method for two dimensional unsteady reacting flows, in: Symposium (International) on Combustion, vol. 16, (1) Elsevier, 1977, pp. 1503–1515, http://dx.doi.org/10.1016/S0082-0784(77)80432-3.
[20] Jean-Jacques Hok, et al., A modeling strategy for the thickened flame simulation of propagating lean hydrogen–air flames, Int. J. Hydrog. Energy 78 (2024) 1133–1141, http://dx.doi.org/10.1016/j.ijhydene.2024.06.298.
[21] Nicola Detomaso, et al., A generalization of the thickened flame model for stretched flames, Combust. Flame 258 (2023) 113080, http://dx.doi.org/10.1016/j.combustflame.2023.113080.
[22] A. Aniello, et al., Introducing thermodiffusive effects in large-eddy simulation of turbulent combustion for lean hydrogen-air flames, in: Center for Turbulence Research, Proceedings of the Summer Program, 2022, pp. 267–277.
[23] Daniel Connell Haworth, Progress in probability density function methods for turbulent reacting flows, Prog. Energy Combust. Sci. 36 (2) (2010) 168–259, http://dx.doi.org/10.1016/j.pecs.2009.09.003.
[24] Olivier Soulard, Approches PDF pour la combustion turbulente, prise en compte d'un spectre d'échelles turbulentes dans la modélisation du micromélange et élaboration d'une méthode de Monte Carlo eulérienne (Ph.D. thesis), Rouen, 2005, URL http://www.theses.fr/2005ROUES003.
[25] Luis Valiño, A field Monte Carlo formulation for calculating the probability density function of a single scalar in a turbulent flow, Flow, Turbul. Combust. 60 (2) (1998) 157–172, http://dx.doi.org/10.1023/A:1009968902446.
[26] Luis Valino, Radu Mustata, Khaled Ben Letaief, Consistent behavior of Eulerian Monte Carlo fields at low Reynolds numbers, Flow, Turbul. Combust. 96 (2016) 503–512, http://dx.doi.org/10.1007/s10494-015-9687-0.
[27] E. Æsøy, James R. Dawson, TNF workshop, 2023, URL https://tnfworkshop.org/bluff-body-hydrogen-flame-ntnu-trondheim/.
[28] Antonio Masucci, et al., Numerical investigation of premixed and non-premixed hydrogen flames using large-eddy simulations and flamelet models, ASME J. Eng. Gas Turbines Power 144 (9) (2025) 091014, http://dx.doi.org/10.1115/1.4069451.
[29] Gregory S. Jackson, et al., Influence of H2 on the response of lean premixed CH4 flames to high strained flows, Combust. Flame 132 (3) (2003) 503–511, http://dx.doi.org/10.1016/S0010-2180(02)00496-0.
[30] Eun-Seong Cho, Suk Ho Chung, Improvement of flame stability and NO x reduction in hydrogen-added ultra lean premixed combustion, J. Mech. Sci. Technol. 23 (2009) 650–658, http://dx.doi.org/10.1007/s12206-008-1223-x.
[31] Alessandro Porcarelli, Boris Kruljević, Ivan Langella, Suppression of NOx emissions by intensive strain in lean premixed hydrogen flamelets, Int. J. Hydrog. Energy 49 (2024) 413–431, http://dx.doi.org/10.1016/j.ijhydene.2023.08.110.
[32] M. Vilespy, et al., Analysis of the origin of NOx emissions in non premixed dual swirl hydrogen flames, Combust. Flame 273 (2025) 113925, http://dx.doi.org/10.1016/j.combustflame.2024.113925.
[33] Michael C. Drake, Richard J. Blint, Thermal NOx in stretched laminar opposed-flow diffusion flames with CO/H2/N2 fuel, Combust. Flame 76 (2) (1989) 151–167, http://dx.doi.org/10.1016/0010-2180(89)90064-3.
[34] Daoguan Ning, Aiwu Fan, Hong Yao, Effects of fuel composition and strain rate on NO emission of premixed counter-flow H2/CO/air flames, Int. J. Hydrog. Energy 42 (15) (2017) 10466–10474, http://dx.doi.org/10.1016/j.ijhydene.2016.12.059.
[35] D.R. Stull, H. Prophet, JANAF Thermochemical Tables, second edition, National Institute of Standards and Technology, Gaithersburg, MD, 1971, http://dx.doi.org/10.6028/NBS.NSRDS.37.
[36] Lukas Berger, et al., Effects of karlovitz number variations on thermodiffusive instabilities in lean turbulent hydrogen jet flames, Proc. Combust. Inst. 40 (1–4) (2024) 105219, http://dx.doi.org/10.1016/j.proci.2024.105219.
[37] Mohamad Fathi, et al., Effects of intense strain on flame structure and NOx generation in turbulent counterflow lean-premixed hydrogen flames, Combust. Flame 282 (2025) 114459, http://dx.doi.org/10.1016/j.combustflame.2025.114459.
[38] T. Poinsot, D. Veynante, Theoretical and Numerical Combustion, Edwards, ISBN: 9781930217102, 2005, URL https://books.google.it/books?id=cqFDkeVABYoC.
[39] T. Brauner, W.P. Jones, A.J. Marquis, LES of the cambridge stratified swirl burner using a sub-grid pdf approach, Flow, Turbul. Combust. 96 (2016) 965–985, http://dx.doi.org/10.1007/s10494-016-9719-4.
[40] Edward E. Gao, A large-eddy simulation scheme for turbulent reacting flows, Phys. Fluids A: Fluid Dyn. 5 (6) (1993) 1282–1284, http://dx.doi.org/10.1063/1.858617.
[41] César Dopazo, Edward E. Obrien, Functional formulation of nonisothermal turbulent reactive flows, Phys. Fluids 17 (11) (1974) 1968, http://dx.doi.org/10.1063/1.1694652.
[42] W.P. Jones, A.J. Marquis, V.N. Prasad, LES of a turbulent premixed swirl burner using the Eulerian stochastic field method, Combust. Flame 159 (10) (2012) 3079–3095, http://dx.doi.org/10.1016/j.combustflame.2012.04.008.
[43] W.P. Jones, S. Navarro-Martinez, O. Röhl, Large eddy simulation of hydrogen auto-ignition with a probability density function method, Proc. Combust. Inst. 31 (2) (2007) 1765–1771, http://dx.doi.org/10.1016/j.proci.2006.07.041.
[44] Eindhoven University of Technology, CHEM1D. A one dimensional laminar flame code, 2021.
[45] A.G. Iyer, Investigation of Unsteady Stretch Effects Using Premixed Counterflow Flames (Ph.D. thesis), Technische Universiteit Eindhoven, Mechanical Engineering, ISBN: 978-90-386-4453-0, 2018, Proefschrift.
[46] E. Æsøy, et al., Acoustic-convective interference in transfer functions of methane/hydrogen and pure hydrogen flames, J. Eng. Gas Turbine Power 143 (2021) 121017/1–121017/10, http://dx.doi.org/10.1115/1.4051960.
[47] Michael P. Burke, et al., Comprehensive H2/O2 kinetic model for high-pressure combustion, Int. J. Chem. Kinet. 44 (7) (2012) 444–474, http://dx.doi.org/10.1002/kin.20603.

[48] T. Capurso, et al., NOx pathways in lean partially premixed swirling H2-air turbulent flame, Combust. Flame 248 (2023) 112581, http://dx.doi.org/10.1016/j.combustflame.2022.112581.
[49] Maria Rosaria Acquaviva, Alessandro Porcarelli, Ivan Langella, Influence of soret effect on flame structure and NOx emissions in highly strained lean premixed counterflow hydrogen flames, Fuel 395 (2025) 134939, http://dx.doi.org/10.1016/j.fuel.2025.134939.
[50] I.B. Celik, Z.N. Cehreli, I. Yavuz, Index of resolution quality for large eddy simulations, J. Turbomach. (2005) http://dx.doi.org/10.1115/1.1990201.
[51] Ivan Langella, Large Eddy Simulation of Premixed Combustion Using Flamelets (Ph.D. thesis), Apollo - University of Cambridge Repository, 2016, http://dx.doi.org/10.17863/CAM.14139.
[52] Reo Kai, et al., LES flamelet modeling of hydrogen combustion considering preferential diffusion effect, Int. J. Hydrog. Energy 48 (29) (2023) 11086–11101, http://dx.doi.org/10.1016/j.ijhydene.2022.12.164.
[53] Alessandro Porcarelli, Ivan Langella, Mitigation of preferential diffusion effects by intensive strain in lean premixed hydrogen flamelets, Proc. Combust. Inst. 40 (1–4) (2024) 105728, http://dx.doi.org/10.1016/j.proci.2024.105728.
[54] Shuguo Shi, et al., Assessing turbulence–flame interaction of thermo-diffusive lean premixed H2/air flames towards distributed burning regime, Combust. Flame 269 (2024) 113699, http://dx.doi.org/10.1016/j.combustflame.2024.113699.
[55] C.K. Law, Combustion Physics, Cambridge University Press, ISBN: 9781139459242, 2010, URL https://books.google.it/books?id=vWgJvKMXwQ8C.